This is an open access article published under an ACS AuthorChoice License, which permits copying and redistribution of the article or any adaptations for non-commercial purposes.

ACS OMEGA

http://pubs.acs.org/journal/acsodf

Article

Mechanically Robust and Flame-Retardant Silicon Aerogel Elastomers for Thermal Insulation and Efficient Solar Steam Generation

Chao Liu, Shujuan Wu, Zifeng Yang, Hanxue Sun, Zhaoqi Zhu, Weidong Liang, and An Li*

Cite This: *ACS Omega* 2020, 5, 8638–8646

Read Online

ACCESS | Metrics & More | Article Recommendations | Supporting Information

ABSTRACT: In this work, we report the synthesis of silicon aerogel elastomers (SAEs) by one-pot hydrolytic condensation of silanes, followed by drying at room temperature. The as-synthesized SAE features excellent flexibility and mechanical robustness, for example, a high compressive strength of up to 40 kPa at 75% strain was achieved. Combined with their thermal insulation properties (a low thermal conductivity of *ca.* 0.02 W m^{-1} K^{-1} in air), for the first time, such SAEs were used as a porous platform for both flame-retardant measurement and solar steam generation. By coating with $Mg(OH)_2$ via a facile coprecipitation method, the treated SAEs show excellent flame retardancy with a peak heat release rate of 25.61 kW m^{-2}, in addition to high fire resistance and excellent smoke suppression. When used as a solar steam generator, their evaporation efficiency was measured to be 82.7% (1 kW m^{-2}), which could compete with that of other high-performance bilayered photothermal materials reported so far. Taking advantage of their simple and cost-efficient manufacture and superior mechanical robustness and flexibility, such SAEs with multifunctionalities may have great potential for a wide variety of energy-saving applications, for example, especially for thermal insulation coatings with better flame retardancy and efficient solar steam generation for desalination or freshwater production.

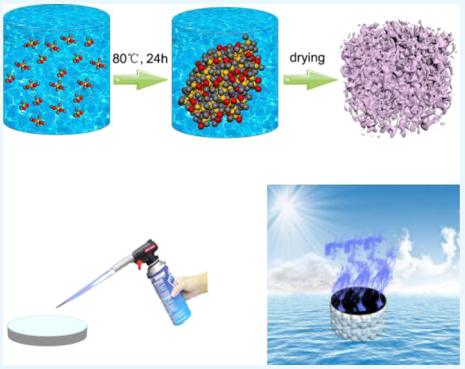

INTRODUCTION

Micro- or nanoporous materials have been the subject of intense interest for both industrial and academic communities for a great variety of applications.[1,2] Among them, aerogels, which usually have very low apparent densities and large specific surface areas, have attracted extensive attention.[3,4] To date, a number of aerogels have been developed,[5−16] including carbon-based aerogels, organic aerogels, and inorganic aerogels. Silicon aerogels are one of the most famous candidates known as excellent thermal insulators owing to their larger open pores, high porosity with inner surface areas, and extremely low thermal conductivity.[17,18] In addition, silicon aerogels can be easily manufactured in monolithic shape, which thus endows them with good practical processability. Until now, silicon aerogels have found useful applications[19,20] in building thermal insulation, solar energy saving, spacecraft, and optical applications. However, unfortunately, silicon aerogels are usually brittle and fragile in nature, which corresponds to their weak three-dimensional framework structure that consists of necklace-like connection of silica particles. Such poor mechanical properties dramatically impair their processability and thus restrict their widespread applications.[21,22] So far, a variety of methods have been employed to improve the mechanical properties of silicon aerogels, including chemical cross-linking, doping with nanofillers, template methods, and so forth; however, these methods usually have their respective drawbacks such as expensive or complicated multistep manufacture.[23,24] In many cases, the improvement of mechanical properties of silicon aerogels by these methods comes at the cost of sacrificing their other functionalities, for example, increase of densities and thermal conductivity or decrease of porosity and specific surface area.[25−28] Worse still, in some cases, these modified silicon aerogels or hybrid silicon aerogels incorporated with polymers or nanofillers, on the other hand, show a dramatic decrease in their flame retardancy because of the flammable nature of the organics or carbon-based fillers, making them unsuitable for thermal insulation,[29,30] especially in building construction and other special applications, for example, flame retardants[31−33] and solar steam generation.[34,35] Thus, the exploitation of a simple but efficient approach to enhance their mechanical properties is urgently needed.

In this work, we report the synthesis of silicon aerogel elastomers (SAEs) with excellent mechanical robustness and flexibility by one-pot hydrolytic condensation of silanes, followed by drying at room temperature. Combined with their

Received: January 7, 2020
Accepted: March 24, 2020
Published: April 6, 2020

ACS Publications

© 2020 American Chemical Society

https://dx.doi.org/10.1021/acsomega.0c00086
ACS Omega 2020, 5, 8638–8646

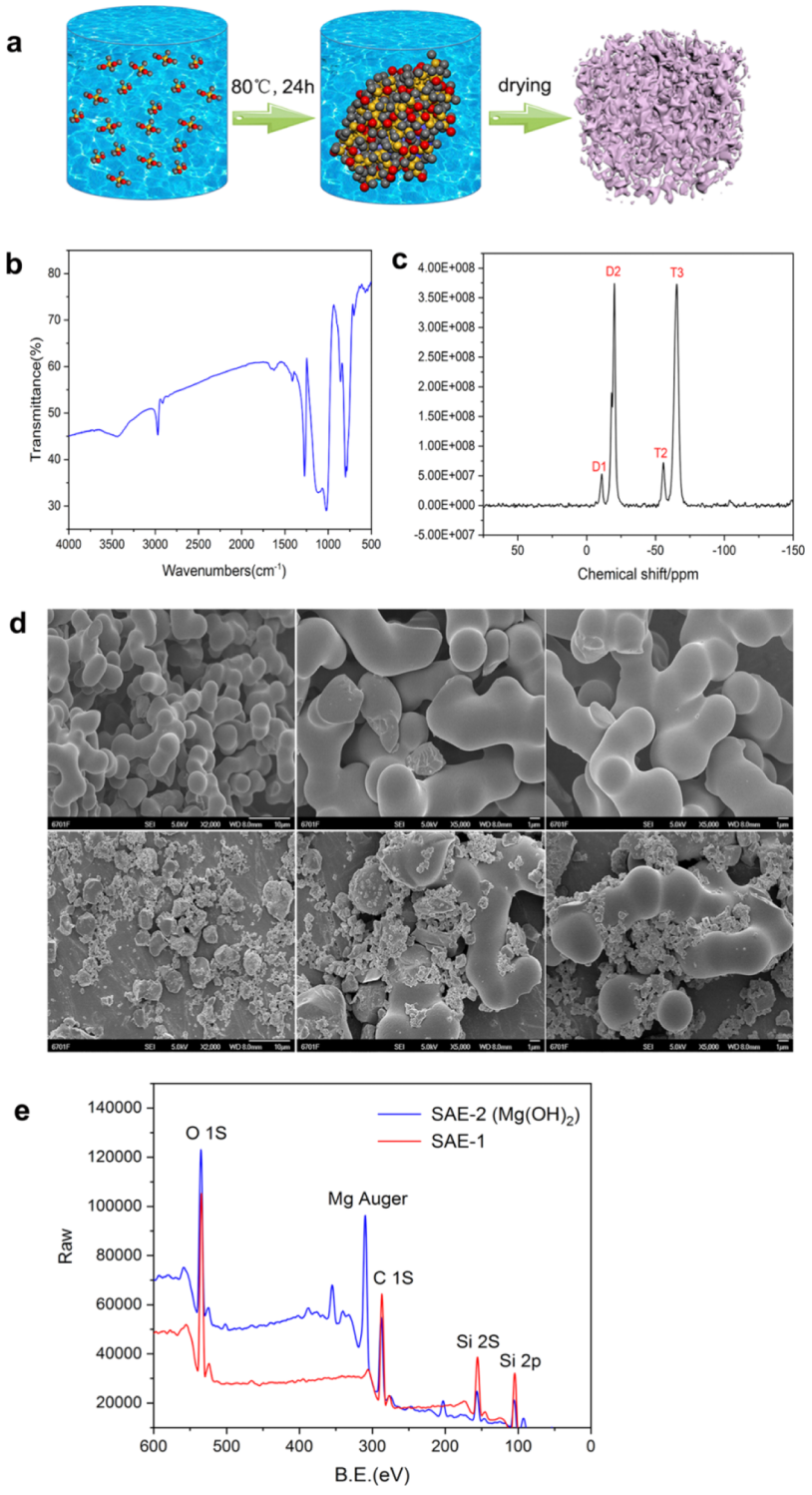

Figure 1. (a) Schematic diagram of the synthesis of the SAE. (b) FTIR spectra of the SAE. (c) Solid-state ^{29}Si NMR spectrum of the SAE. (d) SEM images of the unmodified SAE (above, scale bar: 10 μm for the left picture and 1 μm for the middle and right picture) and modified SAE (below, scale bar: 10 μm for the left picture and 1 μm for the middle and right picture). (e) XPS spectra of SAE-1 and $Mg(OH)_2$-treated SAE-2.

low thermal conductivity of *ca.* 0.02 W m^{-1} K^{-1} in air, the as-synthesized SAEs show excellent flame retardancy and high steam generation efficiency. To our knowledge, the employment of such SAEs as a porous platform as either flame retardants or solar steam generators has never been reported so far. The findings of this work, however, may open a new possibility for the future creation of multifunctional silicon aerogels with enhanced mechanical properties for a great variety of applications, for example, thermal insulation coatings, solar steam generation for desalination or freshwater production, and so on.

MATERIALS AND METHODS

Materials. Acetic acid and urea were purchased from Sinopharm Chemical Reagent Co., Ltd., and the surfactant *n*-

https://dx.doi.org/10.1021/acsomega.0c00086
ACS Omega 2020, 5, 8638−8646

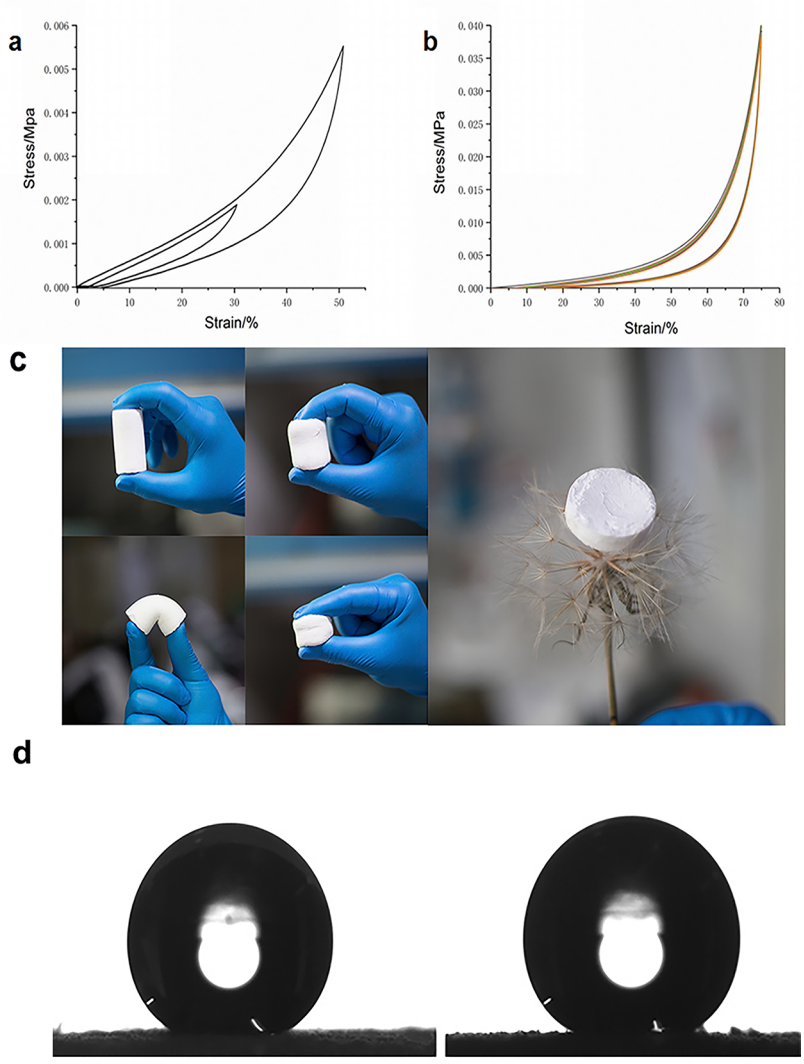

Figure 2. Mechanical properties of the SAE. (a) Compressive σ *vs* ε curves during loading −unloading cycles with increasing ε amplitude. (b) 10-cycle fatigue test with a compressive ε of 75%. (c) Camera photographs of compression and bending of the SAE. (d) Water CA of SAE-1 and SAE-2.

hexadecyltrimethylammonium chloride (CTAC) was obtained from J & K. Dimethyldimethoxysilane (DMDMS) and methyltrimethoxysilane (MTMS) were purchased from Macklin. All of the chemical reagents were used as received without further purification.

Methods. *Preparation of SAE-1.* SAEs were synthesized through a facile one-pot reaction. Typically, aqueous acetic acid solution (15 mL, 5 mM), urea (5.0 g), and the surfactant CTAC (0.80 g) were added into a glass test tube, followed by adding MTMS (3.0 mL) and DMDMS (2.0 mL) under vigorous stirring at ambient temperature for 60 min until a homogeneous solution was achieved. After transferring the as-obtained sol into a tight SAE container, the reaction system was transferred into a forced convection oven and the mixture was heated at 80 °C for 24 h until complete gelation and aging. After that, the as-prepared products (gels) were washed with methanol several times followed by soaking and squeezing several times to ensure the complete removal of the residual impurities. Then, the xerogels were obtained after drying the samples under ambient conditions.

Preparation of SAE-2. The purpose is to treat a layer of magnesium hydroxide flame-retardant coating on the surface of silicon aerogels. This method of synthesizing SAE-2 is similar to the layer-by-layer method. A solution of 1.425 g of magnesium chloride was weighed into a solution using a beaker. Another beaker was taken and 1.2 g of sodium hydroxide was weighed to be dissolved. The assembly process is as follows: first, the silicon aerogel was immersed into the magnesium chloride solution for 5 min, and the excess magnesium chloride solution was washed away with deionized water; then, the sample was immersed into the sodium hydroxide solution for 5 min, and the excess sodium hydroxide solution was washed again with deionized water. The above process is a loop. After treatment, the weight increase is found to be about 28%.

Characterization. The morphologies of SAE aerogels were analyzed by scanning electron microscopy (SEM, JSM-6701F, JEOL, Ltd.) ^{13}C cross-polarization/magic angle spinning NMR spectra were recorded using a 400 MHz solid-state nuclear magnetic analyzer test. Fourier transform infrared (FTIR) spectra were recorded on a Nexus 670 spectrum instrument. The TDA curves of the samples were tested by thermogravimetric analysis (TGA, PerkinElmer) at a heating rate of 10 °C min^{-1} under a nitrogen/air atmosphere. The measurement of powder X-ray diffraction patterns was performed on a D/Max-2400 X-ray diffractometer (Rigaku Miniflex, Japan) using Cu Kα radiation at 40 kV and 100 mA from 2 to 80°. The contact angle

https://dx.doi.org/10.1021/acsomega.0c00086
ACS Omega 2020, 5, 8638−8646

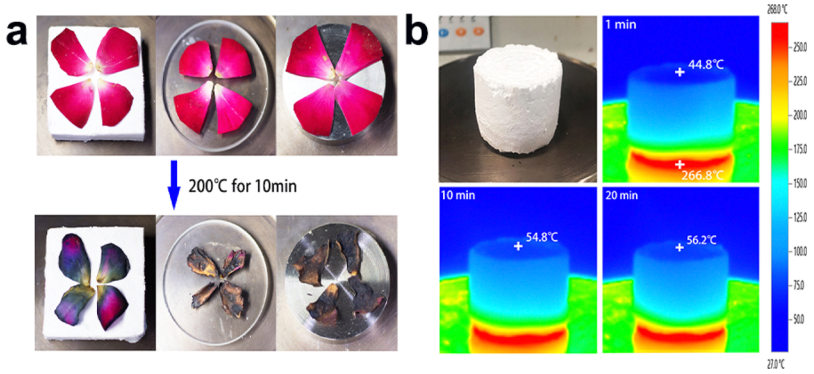

Figure 3. Thermal insulation properties of the SAE. (a) Thermal insulation capacity of the SAE compared with that of Fe and glass materials for protecting fresh petals from withering. (b) Optical and IR images of the SAE on a 200 °C heating stage for 20 min.

(CA) of water samples was measured using a CA meter (DSA100, Kruss). The thermal conductivity of the samples was measured using a multifunction rapid thermal conductivity tester (DRE-III, China). The torch burn test was conducted by exposing the sample to direct flame produced from a butane torch at a 45° angle for 10 s. Both the horizontal flame test (HFT) and cone calorimetry (CONE) tests were performed according to our previous work.[36] X-ray photoelectron spectroscopy (XPS) analyses of the SAE were performed using an ESCALAB 250Xi X-ray photoelectron spectrometer. A Ux50 high speed camera was purchased from Chengdu Tusheng Technology Co., Ltd. The SAE surface was illuminated with a solar simulator (xenon arc lamp, CEL-S500, Ceaulight) equipped with a solar filter (AM 1.5, Ceaulight). The temperature of the sample surface was observed using an IR thermal camera (Thermal Imager TESTO 869, Testo SE & Co. KGaA, Germany). The solar steam generation measurement is performed according to our previous study[12] (the experiment was performed at 22.5 °C, experiment humidity was 40%, and wind speed was almost zero throughout the experiment).

RESULTS AND DISCUSSION

Fabrication and Structure Characterizations of SAE-1 and SAE-2. As shown in Figure 1a, we have prepared SAEs using methyltrimethoxysilane (MTMS) and dimethyldimethoxysilane (DMDMS) as precursors through a simple one-pot method. The molecular level structures of SAEs were analyzed by FTIR, and the FTIR spectra of SAEs are shown in Figure 1b. The peaks at 840−670 cm^{-1} are ascribed to the telescopic vibration of Si and C. The peaks at 1090−920 cm^{-1} are ascribed to the stretching vibration of Si−O, and the absorption peaks in the range 1340−1270 cm^{-1} are attributed to the C−H bending vibration. The peaks at 2920 cm^{-1} are assigned to the C−H stretching vibration, indicating that the compound contains $-CH_3$. The structures of SAE were further confirmed with the solid-state ^{29}Si NMR spectrum, as shown in Figure 1c. D^1 confirms to Si species with one siloxane bond, and D^2 confirms to fully condensed Si species of DMDMS. T^2 confirms to condensed Si species with two siloxane bonds, and T^3 confirms to fully condensed Si species of MTMS. The SEM images of SAE-1 and SAE-2 are shown in Figure 1d. It can be seen that SAE-1 is composed of interconnected irregular spheres with a diameter in the range of 1.7−2.1 μm. In addition, the surface morphology of SAE-1 spheres is much smoother than that of SAE-2. At the same time, the SEM image clearly shows that the surface of SAE-2 is extremely rough, and we initially judged that this was mainly due to the accumulation of magnesium hydroxide particles in the structure of spherical SAEs. Furthermore, both the SAE samples have a porous three-dimensional network structure where interpenetrated pores with nanometer size are present in the materials. In order to verify our conjecture, the chemical composition of SAE samples was measured by XPS. The XPS spectra of SAE-1 and $Mg(OH)_2$-treated SAE-2 are shown in Figure 1e. In the XPS spectra, peaks appear at 540, 280, 160, and 108 eV, indicating that both SAE-1 and SAE-2 contain the carbon element, silicon, and oxygen. SAE-2 did not lose these conventional elements because of postprocessing. After treatment of SAE-2 with $Mg(OH)_2$, the combination of the binding energy at 308 eV in SAE-2 is the characteristic peak of magnesium, which confirms our previous conjecture that magnesium has been successfully incorporated onto the SAE.

Mechanical Properties of SAEs. Unlike conventional silicon aerogels, SAEs are mechanically robust, superelastic, and flexible owing to their unique porous three-dimensional network structure which consists of interpenetrated pores inside silicone. We investigated the mechanical properties of the SAE through uniaxial compression under different strains such as 30, 50, and 75%. As shown in Figure 2a, after compression, the as-prepared SAE can recover its original shape. Besides, it has also shown excellent elasticity under 75% strain. As depicted in Figure 2b, the SAE can be repeatedly compressed at 75% strain for 10 cycles without damage to the structure (Figure 2b), indicating the excellent mechanical property of the SAE. Wettability measurements show that both SAE-1 and SAE-2 interestingly have a superhydrophobic surface with a water CA of 155.6° for SAE-1 (Figure 2d left) and 155.1° (Figure 2d right) for SAE-2. Such superhydrophobicity should be attributed to both the rough structure of the SAE by random aggregation of nanospheres and their inherently hydrophobic chemistry in nature, which may endow them with additional functionality for special applications, for example, as ultralight, self-cleaning, and thermal insulation coatings for exterior wall materials in modern buildings.

Thermal Conductivity. Undoubtedly, the SAE samples feature low thermal conductivity, just similar to the conventional silicon aerogels. Thermal conductivity measurements show that the SAE exhibits a very low thermal conductivity of 19 mW m^{-1} K^{-1} at room temperature. To further intuitively evaluate the thermal insulation property of the SAE, a comparative experiment was performed by heating thick plates made of SAE, iron, and glass on a heating stage at 200 °C, followed by placing fresh petals on top of each plate. As shown in Figure 3a,

https://dx.doi.org/10.1021/acsomega.0c00086
ACS Omega 2020, 5, 8638−8646

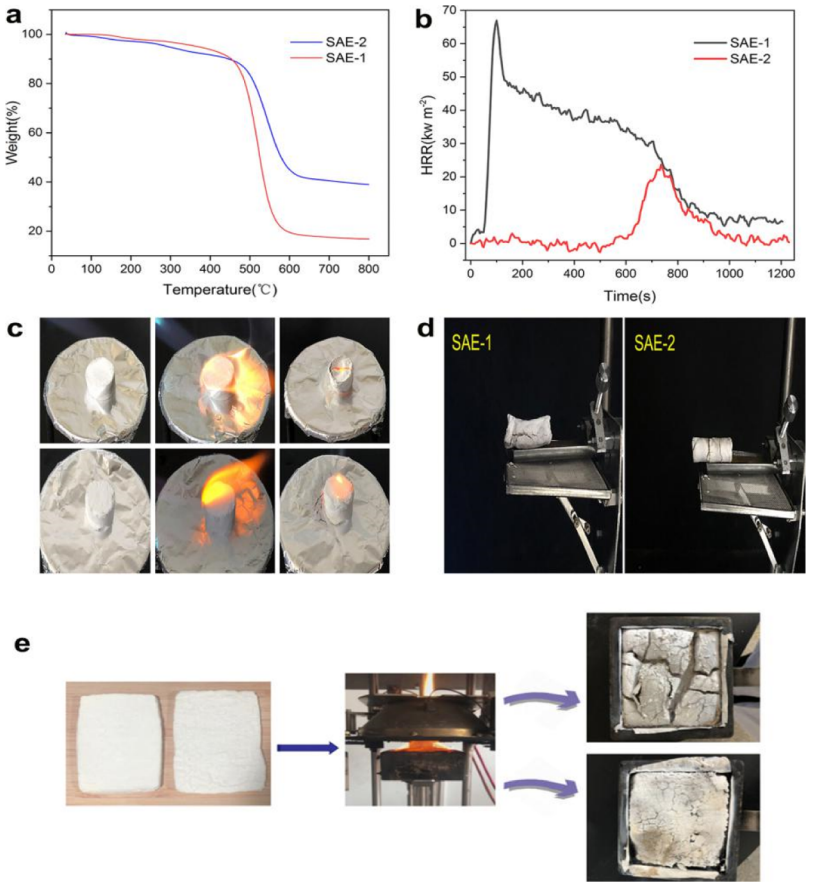

Figure 4. (a) TGA curves of SAE-1 and SAE-2 under nitrogen. (b) HRR curves of pure SAE-1 and SAE-2. (c) Picture of the SAE-1 torch test (above) and pictures of the SAE-2 torch test (below). (d) Digital photos of horizontal burning of SAE-1 (left) and SAE-2 (right). (e) Digital photographs of SAE-2 in the CONE tests.

petals on the SAE showed a slight wilting after 10 min of heating; moreover, the flowers on other plates were burnt and withered, indicating the excellent thermal insulation properties of the SAE. To further detect the dynamic temperature changes of the SAE during heating, an infrared (IR) camera was employed to monitor the changes in surface temperature of the SAE. As shown in Figure 3b, observing the temperature gradient of the SAE heating plate, the top temperature of the SAE was maintained at around 45 °C, after being placed on a 200 °C heating stage for 1 min, and the temperature increased to about 55 °C at about 10 min of heating and then remained constant at 20 min of heating. These also prove that SAEs have strong thermal insulation properties.

Fire Resistance. The thermal stabilities of SAE-1 and SAE-2 were investigated by TGA under a nitrogen atmosphere. As shown in Figure 4a, both SAE-1 and SAE-2 show an initial decomposition temperature of about 400 °C, indicating excellent thermal stability. When the temperature was increased up to 300 °C, only a small weight loss of 10% for both SAE-1 and SAE-2 was observed. The weight loss for both SAE-1 and SAE-2 increased with the increase of temperature, for example, the weight loss reaches 83.15% for SAE-1 and 60.99% for SAE-2 at 800 °C. Meanwhile, it is obvious that the thermal stability of SAE-2 is better than that of SAE-1. The CONE test is an effective test for simulating materials in real fires, which could offer main parameters, for example, heat release rate (HRR) and total heat release (THR). The peak value of HRR (pHRR) is one of the most important factors for indicating the fire safety, which displays the moment when the heat of a fire is likely to ignite adjacent objects and further propagate. In this work, the CONE test was performed to provide data on evaluation of the combustion properties of SAE-1 and SAE-2 by measuring the HRR, THR, and pHRR. All information is shown in Figure 4b,e. From the HRR curves of SAE-1, we can see that its values increase sharply even at the initial stage and reaches up to 67.23 kW m^{-2} quickly, reflecting that SAE-1 burns quickly after ignition. For SAE-2, its pHRR value was measured to be 25.61 kW m^{-2}, which is 61.9% lower than that of SAE-1. As a result, SAE-2 shows more flame stability than SAE-1, further suggesting that the trace amounts of $Mg(OH)_2$ could dramatically improve the flame retardancy of SAE-2. Moreover, such stronger flame retardancy of SAE-2 than SAE-1 is also in good agreement with the torch test results and the HFT results. The flammability of the SAE was studied through torch burn tests, where the samples are exposed to direct flame produced from a butane torch, as shown in Figure 4c. During the torch burn tests, the SAE samples instantly turned gray without obvious flame by direct exposure to butane flame. After the test, SAE-2 kept its original form and was basically not destroyed, indicating that the SAE-2 structure did not collapse. This result suggests that the surface magnesium oxide coating may provide a strong protective layer and in turn serve as a barrier to prevent heat flow and oxygen diffusion to the substrate material. Meanwhile, SAE-2 was first decomposed into intermediate compounds and water vapor, which is a good smoke suppressant during the combustion process. In order to investigate the flame-retardant performance

https://dx.doi.org/10.1021/acsomega.0c00086
ACS Omega 2020, 5, 8638−8646

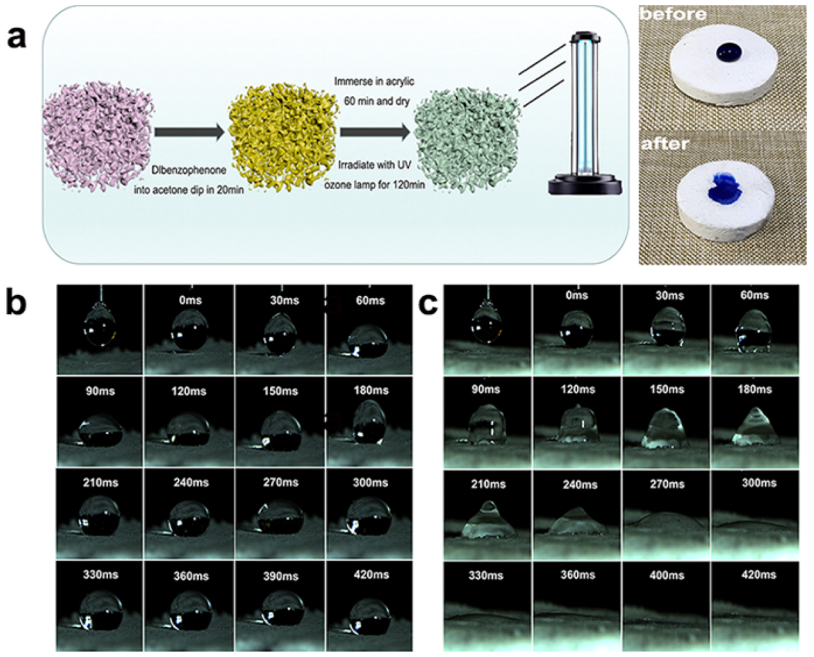

Figure 5. (a) Schematic of SAE-1 for modified and hydrophilic pictures. (b) Camera photos of the droplet impregnation process on the surface of SAE-1. (c) Camera photos of the droplet impregnation process on the surface of the hydrophilic treated C-SAE.

of the sample, horizontal burn tests for both SAE-1 and SAE-2 were also carried out to measure the flame speed. SAE-1 immediately ignited and bright flame can be obviously observed until the combustion was completed, followed by smoldering inside SAE-1 and no residue. The average burn rate for pure SAE-1 was 8.39 mm min^{-1}. After SAE-2 was ignited, it released a yellow flame, followed by smoldering in SAE-2 and release of a small number of fumes. The average burn rate for the SAE-2 was 6.84 mm min^{-1}, lower than that of SAE-1, further indicating better flame retardancy. This result could be attributed to the coated magnesium hydroxide nanoparticles of SAE-2. It is well known that magnesium hydroxide can be thermally decomposed into magnesium oxide, which would provide a natural protective layer for the sample and release water vapor to reduce the surface temperature of the material and suppress the effect of smoke. As a result, by coating of magnesium hydroxide nanoparticles, the flame retardancy of SAE-2 can be significantly improved by comparison with that of SAE-1.

Hydrophilic Modification of the SAE. Taking advantages of their low thermal conductivity, low density, and mechanical flexibility, we believe that the as-prepared SAE sample should be ideal candidates as solar steam generators, according to the criteria for fabrication of these photothermal materials as mentioned in the previous literature.[37−45] However, improvement in surface hydrophilicity of SAE samples is highly needed to this end, as its inherent hydrophobic surface could restrict the flow of aqueous fluids. Here, we introduce a method of permanent hydrophilic modification by treatment with benzophenone and acrylic acid followed by irradiation with an ultraviolet (UV) ozone lamp. As shown in Figure 5a, it is clear that the water droplet, which was placed on the untreated SAE-1 surface, retains its spherical shape, implying hydrophobic surface wettability. In contrast, it could be quickly absorbed into the treated SAE, indicating strong hydrophilic wettability. Furthermore, to gain a high solar light absorption, the treated SAE-1 was also coated with soot carbon (named C-SAE). For C-SAE, the FTIR spectrum of soot carbon on the sample surface is presented in Figure S1 (Supporting Information). To further confirm the wettability of the C-SAE and untreated SAE-1, we recorded the impregnation process for a water droplet using a high-speed video camera and the results are shown in Figure 5b,c. The impregnation process of unmodified SAE-1 is very slow and the droplet hardly penetrates, exhibiting strong hydrophobic properties. In contrast, the treated C-SAE shows superhydrophilic wettability and the droplet can be quickly and fully impregnated within 420 ms. Such superhydrophilicity of the treated C-SAE should be beneficial for rapid water transportation, which may also provide possibility for solar steam generation by combination with its abundant porosity and excellent thermal insulation.[12,40]

SAE as an Efficient Solar Steam Generator. As shown in Figure 6a,b,f, after coating with carbon soot and surface hydrophilic modification, the C-SAE shows a bilayered structure, for example, a black layer on its surface for light absorption (light absorption >97% from the UV to IR region, Supporting Information, Figure S2) and a porous bottom layer based on the silicon aerogel for water transportation and thermal insulation, which is similar to the typical bilayer-structured solar steam generators reported previously.[12,15] In this case, in order to investigate the solar steam generation performance of the C-SAE, the time-dependent mass change of the water being produced from steam generation was measured to calculate evaporation rates and solar energy conversion efficiency under irradiation of the solar simulator with different light intensities according to our previous works.[12,40] As illustrated in Figure 6c, the amount of water evaporated increases with the increase of solar energy. The evaporation rates, which were calculated from the slope of the time-dependent mass change curves, were found to be 1.437 kg m^{-2} h^{-1} under 1 kW m^{-2}, 1.945 kg m^{-2} h^{-1} under 2 kW m^{-2}, and 1.408 kg m^{-2} h^{-1} under 3 kW m^{-2} for the C-SAE-based solar generators under different illuminations, indicating a superior solar evaporation performance. To verify the light-to-heat conversion ability of samples,[42,43] we used an IR camera to monitor the time-dependent temperature change of the C-SAE

https://dx.doi.org/10.1021/acsomega.0c00086
ACS Omega 2020, 5, 8638−8646

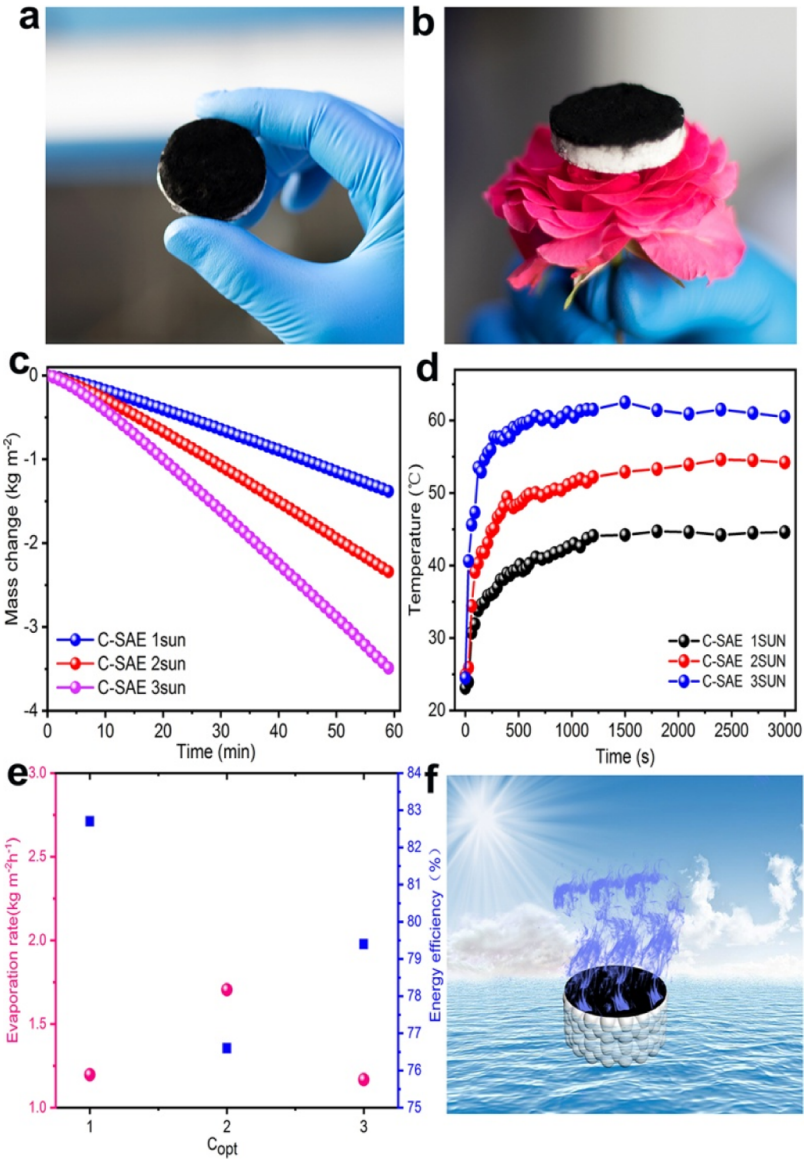

Figure 6. Steam-generation performance and heat-localization behavior of the SAE: (a) Camera photo of the C-SAE. (b) Camera photo of the C-SAE on flowers. (c) Temperature change of the C-SAE surface under different illuminations. (d) Time-dependent mass change of the C-SAE under different illuminations. (e) Evaporation rate and solar steam efficiency of the C-SAE under different illuminations. (f) Schematic of the C-SAE for solar steam generation.

in dry state under 1, 2, and 3 sun illuminations and the results are shown in Figure 6d. Obviously, it can be seen clearly from the curves that the surface temperature of the C-SAE increases sharply under solar irradiation, demonstrating that soot carbon can effectively improve the conversion efficiency of solar energy (Figure 6d). In addition, for a given duration of time, the surface temperature of samples is in the order of 3 > 2 > 1 sun. To obtain the solar energy conversion efficiency of the C-SAE, we also measured its water evaporation rate under a dark environment, 0.234 kg m^{-2} h^{-1}. It is worthwhile to note that the evaporation rate of pure water obtained under a dark environment was subtracted to isolate the effect of solar irradiation on the evaporation rate in all experiments,[44,45] as shown in Figure 6e. The energy conversion efficiency of the C-SAE was calculated to be 82.7, 76.6, and 79.4% under an illumination of 1, 2 and 3 sun, respectively, indicating a better steam-generation performance.

CONCLUSIONS

In summary, we have demonstrated an approach for the fabrication of multifunctional SAEs via one-pot hydrolytic condensation of silanes followed by drying at room temperature. The as-synthesized SAE features excellent mechanical robustness and flexibility, for example, a high compress strength of up to 40 kPa at 75% strain can be obtained, which has great advantages over traditional silicon aerogels usually having poor mechanical properties. Combined with their thermal insulation properties (a low thermal conductivity of *ca.* 0.02 W m^{-1} K^{-1} in air), for the first time, such SAEs were used as a porous platform for both flame-retardant measurement and efficient solar steam generation. By coating with $Mg(OH)_2$ via a facile coprecipitation method, the treated SAE shows excellent flame retardancy with a pHRR of 25.61 kW m^{-2}, in addition to high fire resistance and excellent smoke suppression (see the Supporting Information, Figure S3). In addition, through a hydrophilic modification of the SAEs, the hydrophobic surface wettability of

https://dx.doi.org/10.1021/acsomega.0c00086
ACS Omega 2020, 5, 8638−8646

the C-SAE changes to hydrophilic, which makes them ideal candidates as solar steam generators. As anticipated, the SAE-based solar steam generator shows superior solar steam generation performance with a high energy conversion efficiency of 82.7% under 1 sun illumination. Taking advantage of their simple and cost-efficient manufacture and superior mechanical robustness and flexibility, such SAEs with multifunctionalities may have great potential for a wide variety of energy-saving applications, especially for thermal insulation coatings with better flame retardancy and efficient solar steam generation for desalination or freshwater production.

■ ASSOCIATED CONTENT

Supporting Information

The Supporting Information is available free of charge at https://pubs.acs.org/doi/10.1021/acsomega.0c00086.

Smoke data, UV−vis−NIR absorption spectra, and FT-IR spectra (PDF)

■ AUTHOR INFORMATION

Corresponding Author

An Li − *College of Petrochemical Technology, Lanzhou University of Technology, Lanzhou 730050, P. R. China;* orcid.org/0000-0003-1982-1880; Phone: +86-931-7823125; Email: lian2010@lut.cn; Fax: +86-931-7823125

Authors

Chao Liu − *College of Petrochemical Technology, Lanzhou University of Technology, Lanzhou 730050, P. R. China*

Shujuan Wu − *College of Petrochemical Technology, Lanzhou University of Technology, Lanzhou 730050, P. R. China*

Zifeng Yang − *College of Petrochemical Technology, Lanzhou University of Technology, Lanzhou 730050, P. R. China*

Hanxue Sun − *College of Petrochemical Technology, Lanzhou University of Technology, Lanzhou 730050, P. R. China*

Zhaoqi Zhu − *College of Petrochemical Technology, Lanzhou University of Technology, Lanzhou 730050, P. R. China*

Weidong Liang − *College of Petrochemical Technology, Lanzhou University of Technology, Lanzhou 730050, P. R. China*

Complete contact information is available at: https://pubs.acs.org/10.1021/acsomega.0c00086

Notes

The authors declare no competing financial interest.

■ ACKNOWLEDGMENTS

The authors are grateful to the National Natural Science Foundation of China (grant nos. 21975113, 51962018, 51663012), the Project of Collaborative Innovation Team, Gansu Province, China (grant no. 052005), the Support Program for Hongliu Young Teachers of LUT, the 2019 Key Talent Project of Gansu, and the Innovation and Entrepreneurship Talent Project of Lanzhou (grant no. 2017-RC-33).

■ REFERENCES

(1) Zhan, H.-J.; Wu, K.-J.; Hu, Y.-L.; Liu, J.-W.; Li, H.; Guo, X.; Xu, J.; Yang, Y.; Yu, Z.-L.; Gao, H.-L.; Luo, X.-S.; Chen, J.-F.; Ni, Y.; Yu, S.-H. Biomimetic Carbon Tube Aerogel Enables Super-Elasticity and Thermal Insulation. *Chem* **2019**, *5*, 1871−1882.

(2) Chen, T.; Liu, C.; Mu, P.; Sun, H.; Zhu, Z.; Liang, W.; Li, A. Fatty amines/graphene sponge form-stable phase change material composites with exceptionally high loading rates and energy density for thermal energy storage. *Chem. Eng. J.* **2020**, *382*, 122831.

(3) He, J.; Zhao, G.; Mu, P.; Wei, H.; Su, Y.; Sun, H.; Zhu, Z.; Liang, W.; Li, A. Scalable fabrication of monolithic porous foam based on cross-linked aromatic polymers for efficient solar steam generation. *Sol. Energy Mater. Sol. Cells* **2019**, *201*, 110111.

(4) Chen, T.; Sun, H.; Mu, P.; Zhu, Z.; An, J.; Liang, W.; Li, A. Fatty amines as a new family of organic phase change materials with exceptionally high energy density. *Sol. Energy Mater. Sol. Cells* **2020**, *206*, 110340.

(5) Fu, Y.; Wang, G.; Mei, T.; Li, J.; Wang, J.; Wang, X. Accessible graphene aerogel for efficiently harvesting solar energy. *ACS. Sustain. Chem. Eng.* **2017**, *5*, 4665−4671.

(6) Zhang, W.; Sun, H.; Zhu, Z.; Jiao, R.; Mu, P.; Liang, W.; Li, A. N-doped hard carbon nanotubes derived from conjugated microporous polymer for electrocatalytic oxygen reduction reaction. *Renewable Energy* **2020**, *146*, 2270−2280.

(7) Cao, Z.-J.; Liao, W.; Wang, S.-X.; Zhao, H.-B.; Wang, Y.-Z. Polyurethane foams with functionalized graphene towards high fire-resistance, low smoke release, superior thermal insulation. *Chem. Eng. J.* **2019**, *361*, 1245−1254.

(8) Chen, L.; Xia, M.; Du, J.; Luo, X.; Zhang, L.; Li, A. Superhydrophilic and Oleophobic Porous Architectures Based on Basalt Fibers as Oil-Repellent Photothermal Materials for Solar Steam Generation. *ChemSusChem* **2020**, *13*, 493−500.

(9) Li, T.; Liu, H.; Zhao, X.; Chen, G.; Dai, J.; Pastel, G.; Jia, C.; Chen, C.; Hitz, E.; Siddhartha, D.; Yang, R.; Hu, L. Scalable and highly efficient mesoporous wood-based solar steam generation device: localized heat, rapid water transport. *Adv. Funct. Mater.* **2018**, *28*, 1707134.

(10) Li, X.; Xu, W.; Tang, M.; Zhou, L.; Zhu, B.; Zhu, S.; Zhu, J. Graphene oxide-based efficient and scalable solar desalination under one sun with a confined 2D water path. *Proc. Natl. Acad. Sci. U.S.A.* **2016**, *113*, 13953−13958.

(11) Jiang, Q.; Tian, L.; Liu, K.-K.; Tadepalli, S.; Raliya, R.; Biswas, P.; Naik, R. R.; Singamaneni, S. Bilayered biofoam for highly efficient solar steam generation. *Adv. Mater.* **2016**, *28*, 9400−9407.

(12) Mu, P.; Bai, W.; Fan, Y.; Zhang, Z.; Sun, H.; Zhu, Z.; Liang, W.; Li, A. Conductive hollow kapok fiber-PPy monolithic aerogels with excellent mechanical robustness for efficient solar steam generation. *J. Mater. Chem. A.* **2019**, *7*, 9673−9679.

(13) Mao, J.; Iocozzia, J.; Huang, J.; Meng, K.; Lai, Y.; Lin, Z. Graphene aerogels for efficient energy storage and conversion. *Energy Environ. Sci.* **2018**, *11*, 772−799.

(14) Ni, G.; Zandavi, S. H.; Javid, S. M.; Boriskina, S. V.; Cooper, T. A.; Chen, G. A salt-rejecting floating solar still for low-cost desalination. *Energy Environ. Sci.* **2018**, *11*, 1510−1519.

(15) Guo, A.; Ming, X.; Fu, Y.; Wang, G.; Wang, X. Fiber-based, double-sided, reduced graphene oxide films for efficient solar vapor generation. *ACS Appl. Mater. Interfaces* **2017**, *9*, 29958−29964.

(16) Zhu, L.; Gao, M.; Peh, C. K. N.; Wang, X.; Ho, G. W. Self-Contained Monolithic Carbon Sponges for Solar-Driven Interfacial Water Evaporation Distillation and Electricity Generation. *Adv. Energy Mater.* **2018**, *8*, 1702149.

(17) Yu, Z.-L.; Yang, N.; Apostolopoulou-Kalkavoura, V.; Qin, B.; Ma, Z.-Y.; Xing, W.-Y.; Qiao, C.; Bergström, L.; Antonietti, M.; Yu, S.-H. Fire-retardant and thermally insulating phenolic-silica aerogels. *Angew. Chem., Int. Ed.* **2018**, *57*, 4538−4542.

(18) He, S.; Huang, Y.; Chen, G.; Feng, M.; Dai, H.; Yuan, B.; Chen, X. Effect of heat treatment on hydrophobic silica aerogel. *J. Hazard. Mater.* **2019**, *362*, 294−302.

(19) Aghajamali, M.; Xie, H.; Javadi, M.; Kalisvaart, W. P.; Buriak, J. M.; Veinot, J. G. C. Size and surface effects of silicon nanocrystals in graphene aerogel composite anodes for lithium ion batteries. *Chem. Mater.* **2018**, *30*, 7782−7792.

(20) Chen, K.; Bao, Z.; Shen, J.; Wu, G.; Zhou, B.; Sandhage, K. H. Freestanding monolithic silicon aerogels. *J. Mater. Chem.* **2012**, *22*, 16196−16200.

(21) Henning, S.; Svensson, L. Production of silica aerogel. *Phys. Scripta* **1981**, *23*, 697.

(22) Xu, B.; Wu, H.; Lin, C. X.; Wang, B.; Zhang, Z.; Zhao, X. S. Stabilization of silicon nanoparticles in graphene aerogel framework for lithium ion storage. *RSC Adv.* **2015**, *5*, 30624−30630.
(23) Du, B.; Hong, C.; Wang, A.; Zhou, S.; Qu, Q.; Zhou, S.; Zhang, X. Preparation and structural evolution of SiOC preceramic aerogel during high-temperature treatment. *Ceram. Int.* **2018**, *44*, 563−570.
(24) Li, X.; Feng, J.; Yin, J.; Jiang, Y.; Feng, J. Preparation and Properties of SiBCO Aerogel and Its Composites. *Nanomaterials* **2019**, *9*, 40.
(25) Lamy-Mendes, A.; Silva, R. F.; Durães, L. Advances in carbon nanostructure−silica aerogel composites: a review. *J. Mater. Chem. A.* **2018**, *6*, 1340−1369.
(26) Wang, M.; Liu, F.; Chen, Y.; Gao, J. Fabrication of Macroporous Biomorphic SiC from Cellulose Nanofibers Aerogel. *Materials* **2018**, *11*, 2430.
(27) Hayase, G.; Kanamori, K.; Fukuchi, M.; Kaji, H.; Nakanishi, K. Facile synthesis of marshmallow-like macroporous gels useable under harsh conditions for the separation of oil and water. *Angew. Chem., Int. Ed.* **2013**, *52*, 1986−1989.
(28) Hu, T.; Li, L.; Zhang, J. Green Synthesis of Ant Nest-Inspired Superelastic Silicone Aerogels. *ACS. Sustain. Chem. Eng.* **2018**, *6*, 11222−11227.
(29) Kobayashi, Y.; Saito, T.; Isogai, A. Aerogels with 3D ordered nanofiber skeletons of liquid-crystalline nanocellulose derivatives as tough and transparent insulators. *Angew. Chem., Int. Ed.* **2014**, *53*, 10394−10397.
(30) Hrubesh, L. W.; Poco, J. F. Thin aerogel films for optical, thermal, acoustic and electronic applications. *J. Non-Cryst. Solids* **1995**, *188*, 46−53.
(31) Wang, D.-Y.; Das, A.; Leuteritz, A.; Mahaling, R. N.; Jehnichen, D.; Wagenknecht, U.; Heinrich, G. Structural characteristics and flammability of fire retarding EPDM/layered double hydroxide (LDH) nanocomposites. *RSC Adv.* **2012**, *2*, 3927−3933.
(32) Liao, S.-H.; Liu, P.-L.; Hsiao, M.-C.; Teng, C.-C.; Wang, C.-A.; Ger, M.-D.; Chiang, C.-L. One-step reduction and functionalization of graphene oxide with phosphorus-based compound to produce flame-retardant epoxy nanocomposite. *Ind. Eng. Chem. Res.* **2012**, *51*, 4573−4581.
(33) Apaydin, K.; Laachachi, A.; Ball, V.; Jimenez, M.; Bourbigot, S.; Toniazzo, V.; Ruch, D. Polyallylamine−montmorillonite as super flame retardant coating assemblies by layer-by layer deposition on polyamide. *Polym. Degrad. Stab.* **2013**, *98*, 627−634.
(34) Bae, K.; Kang, G.; Cho, S. K.; Park, W.; Kim, K.; Padilla, W. J. Flexible thin-film black gold membranes with ultrabroadband plasmonic nanofocusing for efficient solar vapour generation. *Nat. Commun.* **2015**, *6*, 10103.
(35) Xu, N.; Hu, X.; Xu, W.; Li, X.; Zhou, L.; Zhu, S.; Zhu, J. Mushrooms as efficient solar steam-generation devices. *Adv. Mater.* **2017**, *29*, 1606762.
(36) Wei, H.; Wang, F.; Sun, H.; Zhu, Z.; Xiao, C.; Liang, W.; Yang, B.; Chen, L.; Li, A. Benzotriazole-based conjugated microporous polymers as efficient flame retardants with better thermal insulation property. *J. Mater. Chem. A* **2018**, *6*, 8633−8642.
(37) Zhu, M.; Li, Y.; Chen, F.; Zhu, X.; Dai, J.; Li, Y.; Yang, Z.; Yan, X.; Song, J.; Wang, Y.; Hitz, E.; Luo, W.; Lu, M.; Yang, B.; Hu, L. Plasmonic Wood for High-Efficiency Solar Steam Generation. *Adv. Energy Mater.* **2018**, *8*, 1701028.
(38) Gao, Y.; Wu, J.; Wang, Q.; Wilkie, C. A.; O'Hare, D. Flame retardant polymer/layered double hydroxide nanocomposites. *J. Mater. Chem. A.* **2014**, *2*, 10996−11016.
(39) Zhu, L.; Gao, M.; Peh, C. K. N.; Ho, G. W. Solar-driven photothermal nanostructured materials designs and prerequisites for evaporation and catalysis applications. *Mater. Horiz.* **2018**, *5*, 323−343.
(40) Fan, Y.; Bai, W.; Mu, P.; Su, Y.; Zhu, Z.; Sun, H.; Liang, W.; Li, A. Conductively monolithic polypyrrole 3-D porous architecture with micron-sized channels as superior salt-resistant solar steam generators. *Sol. Energy Mater. Sol. Cells* **2020**, *206*, 110347.
(41) Raza, A.; Lu, J.-Y.; Alzaim, S.; Li, H.; Zhang, T. Novel receiver-enhanced solar vapor generation: review and perspectives. *Energies* **2018**, *11*, 253.
(42) Zhu, L.; Ding, T.; Gao, M.; Peh, C. K. N.; Ho, G. W. Photothermal Conversion: Shape Conformal and Thermal Insulative Organic Solar Absorber Sponge for Photothermal Water Evaporation and Thermoelectric Power Generation (Adv. Energy Mater. 22/2019). *Adv. Energy Mater.* **2019**, *9*, 1970080.
(43) Yang, M.-Q.; Gao, M.; Hong, M.; Ho, G. W. Visible-to-NIR Photon Harvesting: Progressive Engineering of Catalysts for Solar-Powered Environmental Purification and Fuel Production. *Adv. Mater.* **2018**, *30*, 1802894.
(44) Zhu, L.; Gao, M.; Peh, C. K. N.; Ho, G. W. Recent progress in solar-driven interfacial water evaporation: advanced designs and applications. *Nano Energy* **2019**, *57*, 507−518.
(45) Ding, T.; Zhu, L.; Wang, X.-Q.; Chan, K. H.; Lu, X.; Cheng, Y.; Ho, G. W. Hybrid photothermal pyroelectric and thermogalvanic generator for multisituation low grade heat harvesting. *Adv. Energy Mater.* **2018**, *8*, 1802397.

https://dx.doi.org/10.1021/acsomega.0c00086
ACS Omega 2020, 5, 8638−8646